crystals

MDPI

Article

Anion and Cation Co-Doping of NiO for Transparent Photovoltaics and Smart Window Applications

Chrysa Aivalioti [1,†], Emmanouil G. Manidakis [1,2], Nikolaos T. Pelekanos [1,2], Maria Androulidaki [1], Katerina Tsagaraki [1] and Elias Aperathitis [1,*]

[1] Microelectronics Research Group, Institute of Electronic Structure and Laser, Foundation for Research and Technology—Hellas (FORTH), P.O. Box 1385, 70013 Heraklion, Greece; chrysoula.aivalioti@kaust.edu.sa (C.A.); mman@materials.uoc.gr (E.G.M.); pelekano@materials.uoc.gr (N.T.P.); pyrhnas@physics.uoc.gr (M.A.); ktsag@physics.uoc.gr (K.T.)
[2] Department of Materials Science and Engineering, University of Crete, P.O. Box 2208, 71003 Heraklion, Greece
* Correspondence: eaper@physics.uoc.gr
† Present address: King Abdullah University of Science and Technology (KAUST), Jeddah, Thuwal 23955-6900, Saudi Arabia.

Abstract: Materials engineering based on metal oxides for manipulating the solar spectrum and producing solar energy have been under intense investigation over the last years. In this work, we present NiO thin films double doped with niobium (Nb) and nitrogen (N) as cation and anion dopants (NiO:(Nb,N)) to be used as p-type layers in all oxide transparent solar cells. The films were grown by sputtering a composite Ni-Nb target on room-temperature substrates in plasma containing 50% Ar, 25% O_2, and 25% N_2gases. The existence of Nb and N dopants in the NiO structure was confirmed by the Energy Dispersive X-Ray and X-Ray Photoelectron Spectroscopy techniques. The nominally undoped NiO film, which was deposited by sputtering a Ni target and used as the reference film, was oxygen-rich, single-phase cubic NiO, having a visible transmittance of less than 20%. Upon double doping with Nb and N the visible transmittance of NiO:(Nb,N) film increased to 60%, which was further improved after thermal treatment to around 85%. The respective values of the direct band gap in the undoped and double-doped films were 3.28 eV and 3.73 eV just after deposition, and 3.67 eV and 3.76 eV after thermal treatment. The changes in the properties of the films such as structural disorder, direct and indirect energy band gaps, Urbach tail states, and resistivity were correlated with the incorporation of Nb and N in their structure. The thermally treated NiO:(Nb,N) film was used to form a diode with a spin-coated two-layer, mesoporous on top of a compact, TiO_2 film. The NiO:(Nb,N)/TiO_2heterojunction exhibited visible transparency of around 80%, showed rectifying characteristics and the diode's parameters were deduced using the I-V method. The diode revealed photovoltaic behavior upon illumination with UV light exhibiting a short circuit current density of 0.2 mA/cm^2 and open-circuit voltage of 500 mV. Improvements of the output characteristics of the NiO:(Nb,N)/TiO_2 UV-photovoltaic by proper engineering of the individual layers and device processing procedures are addressed. Transparent NiO:(Nb,N) films can be potential candidates in all-oxide ultraviolet photovoltaics for tandem solar cells, smart windows, and other optoelectronic devices.

Keywords: NiO; NiO co-doping; NiO:(Nb,N); TiO_2; ultraviolet photovoltaic; NiO/TiO_2 heterojunction; urbach tail; sputtering; mesoporous TiO_2; optical properties

Citation: Aivalioti, C.; Manidakis, E.G.; Pelekanos, N.T.; Androulidaki, M.; Tsagaraki, K.; Aperathitis, E. Anion and Cation Co-Doping of NiO for Transparent Photovoltaics and Smart Window Applications. *Crystals* **2024**, *14*, 629. https://doi.org/10.3390/cryst14070629

Academic Editor: Ioannis Spanopoulos

Received: 11 June 2024
Revised: 28 June 2024
Accepted: 1 July 2024
Published: 8 July 2024

1. Introduction

It has been realized that we are experiencing a climatic change. A complete decarbonization of the energy system towards a net-zero future has to be accelerated by employing a clean, renewable energy system for all energy end-use sectors: power, heating/cooling, and transport, securing energy supplies at the same time. Thus, fundamental changes to the way energy is supplied, used, stored, transmitted, bought, and sold, are

necessary to satisfy energy, environmental, and health issues. In addition, it is worth considering that the built environment accounts for more than 45% of the primary energy used in Europe and is responsible for 36% of greenhouse gases [1,2]. This huge amount of energy consumption is mainly due to heating, cooling, and lighting, in residential and commercial buildings, where humans spend almost 90% of their time. Future zero-energy buildings require user-controlled smart windows which can control glare, manage thermal/visual comfort, and at the same time be capable of powering wearable and mobile health indoor sensing systems, including circuits for the Internet of Things (IoT) [3]. Such energy-producing smart windows require the use of transparent solar cells using the ultraviolet (UV) part of the solar spectrum. UV solar radiation accounts for around 7% of the solar spectrum, while the theoretical efficiency of transparent photovoltaics (PV) has been estimated to be 21% [4]. Wide band gap oxide-based semiconductors, with high visible transmittance, can be used for forming the required p-n junction, thus fabricating transparent PVs absorbing the ultraviolet radiation.

Nickel oxide (NiO) is the most commonly used p-type oxide and, provided it can be sufficiently transparent, has been used with transparent n-type oxides such as In_2O_3:Sn (ITO), ZnO, and TiO_2 to form a p/n junction and create solar-blind devices absorbing the ultraviolet solar radiation. All-oxide NiO-based ultraviolet photovoltaics (UV-PVs) have been reported for NiO/TiO_2 [5–9] and NiO/ZnO [10–14]. As in the case of conventional PVs, the main factors determining the conversion efficiency are: (i) the efficient absorption of photons at the front illuminated surface and generation of carriers, (ii) the efficient separation and transfer of these photogenerated carriers across the device with the aid of the built-in electrostatic field at the interface, and (iii) the collection of the photogenerated carriers at the respective electrodes. Three techniques are generally followed to achieve PV with lesser loss mechanisms and higher output characteristics. Firstly, the layers consisting of the PV device are generally deposited/formed on intentionally heated substrates or on unheated substrates followed by post-deposition heat treatments ($\geq$300 °C) so as to create layers with less structural defects, stress and distortion, minimizing thus recombination centers/states for the photogenerated carriers. Secondly, suitable dopants are introduced which, as mentioned above, can reduce structural defects/vacancies, affect the electronic structure, defect levels and the properties of the layers. Thirdly, the insertion of an interlayer at the interface to spatially enhance the built-in electrostatic field and subsequently improve photocurrent and photovoltage [11,15]. For the case of NiO/TiO_2 UV-PVs, improvements in the performance of the devices have been achieved by following some of the above-mentioned techniques. For example, heat treatments up to 600 °C have been employed [9,11], dopants like N in TiO_2 [6] or Nb in NiO [7] have been used or suitable interlayers have been inserted at the NiO-TiO_2 interface such as SnS or MgO [16,17] so as to enhance the output characteristics of the UV-PVs.

In a previous investigation we have shown that nitrogen doping in NiO can improve its transparency by minimizing structural disorder, energy band gap widening [18], and reduction of mid-band-gap states [19]. In addition, it was revealed that p-type Nb-doped NiO can exhibit photovoltaic behavior when forming a p/n junction with mesoporous TiO_2 [7]. In this work, we proceeded in a combinatorial and selective double doping of NiO in an attempt to enhance further the photovoltaic output characteristics of the transparent NiO/TiO_2 heterostructure. The rf-sputtered NiO layer was co-doped with the optimum amounts of anion (nitrogen -N) and cation (niobium -Nb) dopants. The fabricated heterojunction formed with mesoporous TiO_2 showed excellent NiO:(Nb,N)/TiO_2 UV-PV behavior with enhanced characteristics compared to the device where the NiO layer was single doped (NiO:Nb/TiO_2) [7]. Material improvements and modifications of the fabrication procedure of the NiO:(Nb,N)/TiO_2 heterojunction for potential smart windows, transparent electronic, and photonic applications are also addressed.

2. Materials and Methods

2.1. Thin Films Deposition and Device Fabrication

The TiO_2 films were fabricated by the spin-coating technique on Sn_2O_3:F (FTO)-coated glass substrates. The thickness of the glass substrate was 2 mm. Initially, a 40 nm thick compact TiO_2 (c-TiO_2) layer was formed, which was subsequently thermally treated at 500 °C for 15min in ambient air. On top of the c-TiO_2 layer a 200 nm thick mesoporous TiO_2 (m-TiO_2) layer was formed by spin-coating followed by the same heat treatment as the c-TiO_2 layer. The spin-coating conditions of the TiO_2 films have been tabulated in section A in Table 1 and more details can be found in Ref. [19]. The formed m-TiO_2/c-TiO_2 layers and the m-TiO_2/c-TiO_2/FTO/glass substrate will be called hereafter TiO_2 layer/film and TiO_2/FTO/glass substrate, respectively. It should be mentioned that a similar fabrication procedure is used when the TiO_2 is to be used as an electron transfer layer in perovskite solar cells [20]. The TiO_2/FTO/glass substrates were used for depositing the NiO layers to form the heterostructures.

Table 1. Deposition conditions of: (**A**) spin-coated TiO_2 film (m-TiO_2/c-TiO_2) and (**B**) Sputtered NiO-based films.

(A) m-TiO_2/c-TiO_2 Films Details	**Compact TiO_2—c-TiO_2**	**Mesoporous TiO_2—m-TiO_2**
Spin-coating	HCl:C_2H_6O:$C_{12}H_{28}O_4Ti$ = 50 µL:2.3 mL:150 µL	TiO_2paste + C_2H_6O
Rounds per minute/duration (sec)	2000/30	6000/30
Thermal treatment	500 °C/air/15 min	500 °C/air/15 min
Thickness (nm)	40	200
Substrates	FTO/glass (2 mm thick glass)	c-TiO_2/FTO/glass
(B) NiO-based films Details	**NiO—Film X0**	**NiO:(Nb,N)—Film XNN**
Target	Ni	Ni-Nb
Gases flow rates	Ar:O_2 = 50:50	Ar:O_2:N_2 = 50:25:25
Pressure (Pa)	0.67	0.67
Power (W)	300	300
Deposition rate (nm/min)	1.52	1.28
Thickness (nm)	145	130
Target pre-cleaning	300 W/0.67 Pa Ar/45 min	
Substrates	Si (100) pieces, fused silica (1 mm thick), TiO_2/FTO/glass	

The undoped and cation-doped NiO films were fabricated by RF sputtering metallic targets: a Ni target (6 in. diameter, purity 99.99%) for the fabrication of the undoped NiO films, which were used as the reference films, and a Ni-Nb composite target, which consisted of the Ni target with 14 Nb pellets (dia. 1.5 cm × 3 mm thick, 99.95% purity) placed on its surface, for doping the NiO film with niobium [7]. The co-doping of films with the anion dopant was achieved by introducing nitrogen gas in the Ar-O_2 plasma during deposition. The ratios of gases in plasma and the number of Nb pellets used have been shown in previous investigations that could give p-type undoped NiO [21] and single-doped NiO:Nb and NiO:N films with the optimum properties concerning transparency and p-type conduction (see Supplementary Materials) [7,18]. Details of the deposition conditions of the undoped NiO and double-doped NiO:(Nb,N) have been tabulated in section B in Table 1. All sputtered films were deposited on unheated substrates, which were placed 10 cm vertically above the target. The thickness of the films was measured by a profilometer (Veeco Dektak 150). The nickel oxide films were post-deposition thermally treated in a glass tube furnace for 15 min at 300 °C in flowing nitrogen, named thereafter as TT1.

The NiO:(Nb,N)/TiO_2 heterostructures were fabricated by placing the TiO_2/FTO/glass substrates in the sputtering chamber for the deposition of the NiO:(Nb,N) thin films using the sputtering conditions described in section B in Table 1. As ohmic contacts, sputtered Au metal was used for both NiO:(Nb,N) and FTO layers, employing a shadow mask which

defined the junction area (7.8×10^{-3}cm^2). The structure configuration of the fabricated NiO:(Nb,N)/TiO_2 heterodiodes can be seen in Figure 1. The diodes were characterized just after fabrication (as-prepared) and after thermal treatment TT1 (300 °C, N_2, 15 min).

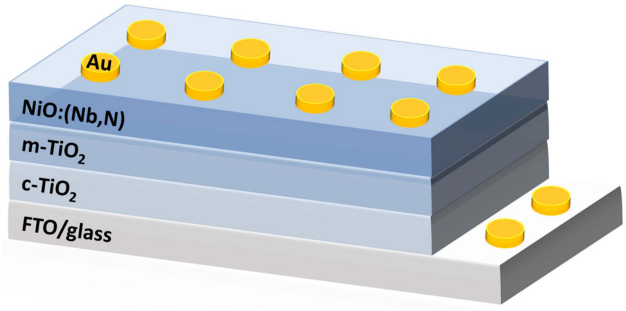

Figure 1. Structure configuration of the fabricated NiO:(Nb,N)/TiO_2 heterodiodes [NiO:(Nb,N)/m-TiO_2/c-TiO_2/FTO/glass]. Thicknesses are not to scale.

2.2. Characterization Methods of Thin Films and Devices

The grazing incidence X-ray diffraction (GIXRD) method was used for studying the crystallinity (crystallographic phases, crystallite size, and lattice strain) of the films. The measurements were performed using a Rigaku D-max 2000 system. The X-ray source was the Cu $K_\alpha 1$ radiation (λ = 1.5406 Å) and the measurement was performed at grazing incidence (1.6°) at a 2θ rate of 0.02°/sec over the range of 30–90°. The average crystallite size was estimated from the Scherrer formula:

$$D = k\lambda/\beta_{hkl}\cos\theta \quad (1)$$

and the lattice strain was estimated from the equation [22]:

$$\varepsilon_L = \beta_{hkl}\cot\theta/4 \quad (2)$$

where k is the shape factor 0.94, λ is the wavelength of incident radiation 1.5406 Å, hkl represents the Miller indices of the diffraction plane, β_{hkl} is the full width at half maximum of the diffraction peak and θ is the Bragg angle of the peak.

The surface morphology of the films was examined by Field-Emission Scanning Electron Microscopy (FE-SEM) employing the Jeol JSM-7000F (Japan) electron microscope, which was equipped with an Energy-Dispersive X-ray (EDX) spectroscopy system (Oxford Instrument-INCA (U.K.)) for elemental analysis of the films. The roughness of the films was examined by the Atomic Force Microscopy (AFM) employing the Digital Instrument-Multimode system (U.K.) (tapping mode operation).

The confirmation of the co-existence of the dopants Nb and N in the Ni-O structure was achieved by the X-ray Photoelectron Spectroscopy (XPS) technique. The XPS measurements were performed on as-prepared undoped and double-doped NiO films. A Specs Lab (Berlin, Germany) photoelectron spectrometer was employed for recording the wide scan survey (from 0 to 1200 eV binding energies) as well as the high-resolution spectra of Nb 3d and N 1s core levels. The XPS source was Al Kα X-ray source at 13 kV and a power of 200 W. All spectra were calibrated such that the adventitious carbon C 1s main peak is at 284.8 eV. Ex-situ heating of the samples was performed at 100 °C for 5 min prior to the XPS measurements and in-situ etching of their surface for 10 min by 0.75 keV Ar^+ with current density 5 mA/cm^2 in order to remove any adsorbed contaminants which could originate from transferring the sample through ambient conditions.

The normal incidence transmittance in the UV-Vis-NIR spectrum was used for determining the optical properties of the films by employing a Perkin Elmer Lambda 950 system. The optical band gap of the films was extracted through the relationship:

$$T \sim \exp(-\alpha d) \quad (3)$$

and applying the Tauc plot, $[(\alpha hv)^n - vs - hv]$, whereas the Urbach tails width was extracted through the relation [23,24]:

$$\alpha = Cexp(E/E_U) \quad (4)$$

In the above equations: T is the transmittance, which was corrected for the transmittance of the substrate, d is the thickness, α is the absorption coefficient, h is the Planck constant, v is the frequency, n = 2 or 1/2 for direct or indirect band gap, E is the photon energy, C is a constant, and E_U is the Urbach energy.

The resistivity of the films was determined by employing the conventional four-probe Van der Pauw technique on films deposited on glass substrates having cross patterns. The ohmic contacts were formed by depositing Au metal (150 nm thick) by electron gun evaporation. The current-voltage (I-V) characteristics of the heterodiodes were recorded using the Agilent 4200-SCS unit from which the diodes' parameters were extracted following thermionic emission theory from the I-V curve [18,25]. The photo I-V curves were obtained by illuminating the diodes from the back side (glass substrate) with a continuous-wave 325 nm laser (intensity 0.71 W/cm^2). The I-V curves under illumination were recorded by employing the Keithley 2401 SMU instrument (Newark, NJ, USA).

3. Results and Discussion

3.1. Thin Films Properties

3.1.1. Properties of TiO_2 Layer

The TiO_2 layer was used as the n-type layer for the p/n heterojunction investigated in this work. It should be reminded that the TiO_2 layer consisted of a compact c-TiO_2, formed on the FTO/glass substrate, on top of which the mesoporous m-TiO_2 was formed and the heterojunction was illuminated to reveal its photovoltaic behavior. The SEM cross-section of the TiO_2/FTO/glass layers is shown in Figure 2a. The FTO and the m-TiO_2 layers, which were around 600 nm and 200 nm thick, respectively, can be easily seen, whereas the 40 nm thick c-TiO_2 layer, in between the FTO and m-TiO_2 layers, can be hardly discerned in Figure 2a. The RMS roughness of the m-TiO_2 surface, as determined from AFM measurements, was 20 nm, which is a typical value for spin-coated mesoporous TiO_2 films [26], whereas XRD results, not shown here but reported elsewhere, revealed that it consisted of a mixture of anatase and rutile phases [19]. The optical properties of the m-TiO_2/c-TiO_2 layers were determined by treating them as one effective single TiO_2 layer deposited on the FTO/glass substrate. The UV-Vis-NIR transmittance of the TiO_2/FTO/glass configuration has been plotted in Figure 2b along with the transmittance of the FTO/glass substrate. The abrupt increase of transmittance (decrease of absorption) for photons with energy less than 4 eV (more than 310 nm) can be observed and the transmittance reaches its maximum value of around 72% for photons with energy of 3.2 eV (387 nm). The absorption coefficient of the effective TiO_2 layer was calculated from the transmittance data, which were then normalized to the transmittance data of the FTO/glass substrate. Through the Tauc plots seen in Figure 2b the direct and the indirect band gap of the effective TiO_2 layer were determined to be 3.72 eV and 3.28 eV, respectively. The co-existence of direct and indirect band gaps for polycrystalline bi-layers has been previously reported [27,28]. It is worth mentioning that the band gap of TiO_2 layer has been reported in the literature to be a phonon-assisted indirect band gap between 2.7 and 3.4 eV depending on the crystalline structure and oxygen vacancies [26,29–31]. The Urbach energy (E_U), which is an indicator of the disorder and defects in the structure introducing localized states at the edge of the conduction band (tail states width), was extracted from the absorption coefficient and was found to be 211 meV [29,31].These optical properties of the effective TiO_2 layer are of importance since they will be correlated with the optical properties of the NiO films, in order to understand the behavior of the fabricated p/n heterojunction of this work, as will be presented and discussed in the next sections. The TiO_2 layer was too resistive for Hall measurements to be performed.

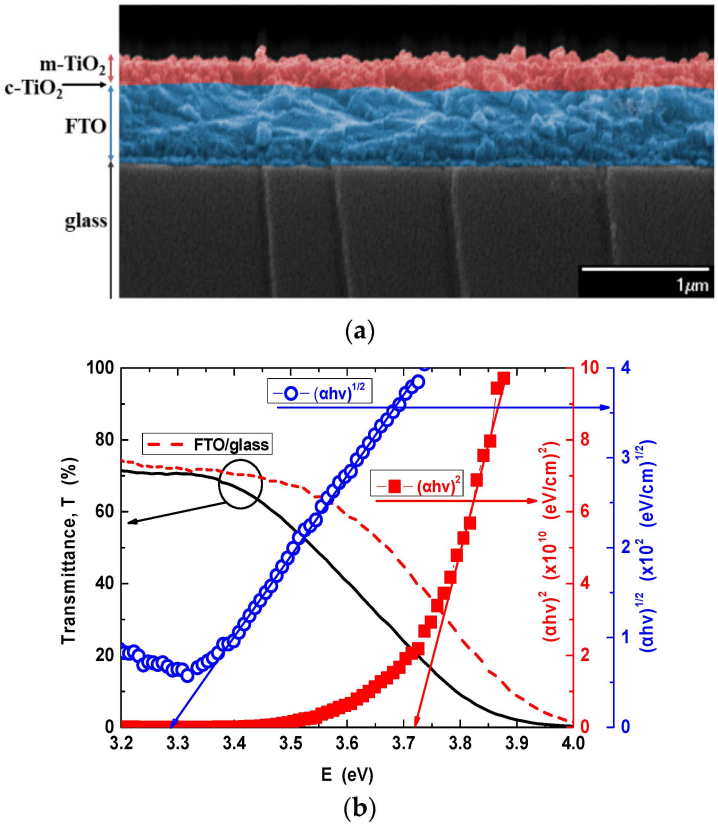

Figure 2. (**a**) SEM cross-sectional image of TiO2/FTO/glass. (**b**) UV-Vis-NIR transmittance of TiO_2/FTO/glass (black solid line) and FTO/glass (red dash lines). The Tauc plots for determining the optical energy gap of effective TiO_2 are also shown in (**b**): blue open circles for indirect band gap ((αhv)1/2-vs-E)) and red solid squares for direct band gap ((αhv)2-vs-E)) analysis.

3.1.2. Properties of NiO and NiO:(Nb,N) Thin Films

The undoped NiO, which was used as the reference X0 film, was deposited following the conditions shown in Table 1. Under these deposition conditions, the NiO films were deposited with a rate of 1.52 nm/min; they were O-rich (at.% O/Ni~1.72) and exhibited p-type behavior [19,21]. In order to simultaneously introduce into the Ni-O structure the optimum amounts of Nb and N as cation and anion dopants, respectively [7,18], Nb pellets were placed on the Ni target surface and N_2 gas replaced half of the O_2 gas used for depositing the undoped NiO film while keeping the %Ar in plasma constant (see section B in Table 1). The resulting film was deposited at a rate of 1.28 nm/min. The reduced deposition rate when compared with the deposition rate of the undoped NiO was due to three factors: (i) the Nb pellets were placed on top of the Ni target thus reducing the exposed Ni target surface to the sputtering plasma, (ii) Nb has a lower sputtering yield than that of Ni, and (iii) the nitrogen atoms are lighter than the oxygen atoms. Even though the existence of cation dopants (Nb) in the Ni-O structure could be revealed through EDX measurements, the light N element could not be accurately detected by EDX and values of less than 1% were at the limit of detection above the noise signal. For these reasons, the existence of Nb and N dopants in the Ni-O structure was also confirmed by XPS experiments. Figure 3a shows the wide-scan XPS spectra of the undoped NiO –X0 film and the double-doped NiO:(Nb,N)—XNN film, in which the characteristic peaks of Ni, O, N, and Nb can be seen, strongly suggesting the presence of both Nb and N in the Ni-O structure. The mild Ar-ion sputtering of the surface, which was performed in situ before the XPS experiment, is known to cause preferential sputtering of species such as oxygen and nitrogen [32,33]. Despite that the nitrogen signal in the XPS wide scan spectra can be clearly observed in the double-doped XNN film the high-resolution spectra of the N 1s

core level was monitored and plotted in Figure 3b. The incorporation of Nb into the Ni-O structure was confirmed by monitoring the high-resolution spectra of the Nb 3d core level, which is seen in Figure 3c. The features at 209.1 eV of the Nb $3d_{3/2}$ peak and 206.6 eV of the Nb $3d_{5/2}$ peak, seen in Figure 3c, indicated that Nb exists in Ni-O structure and is fully oxidized into its maximum valence of +5 (Nb^{5+}) [7,34,35].

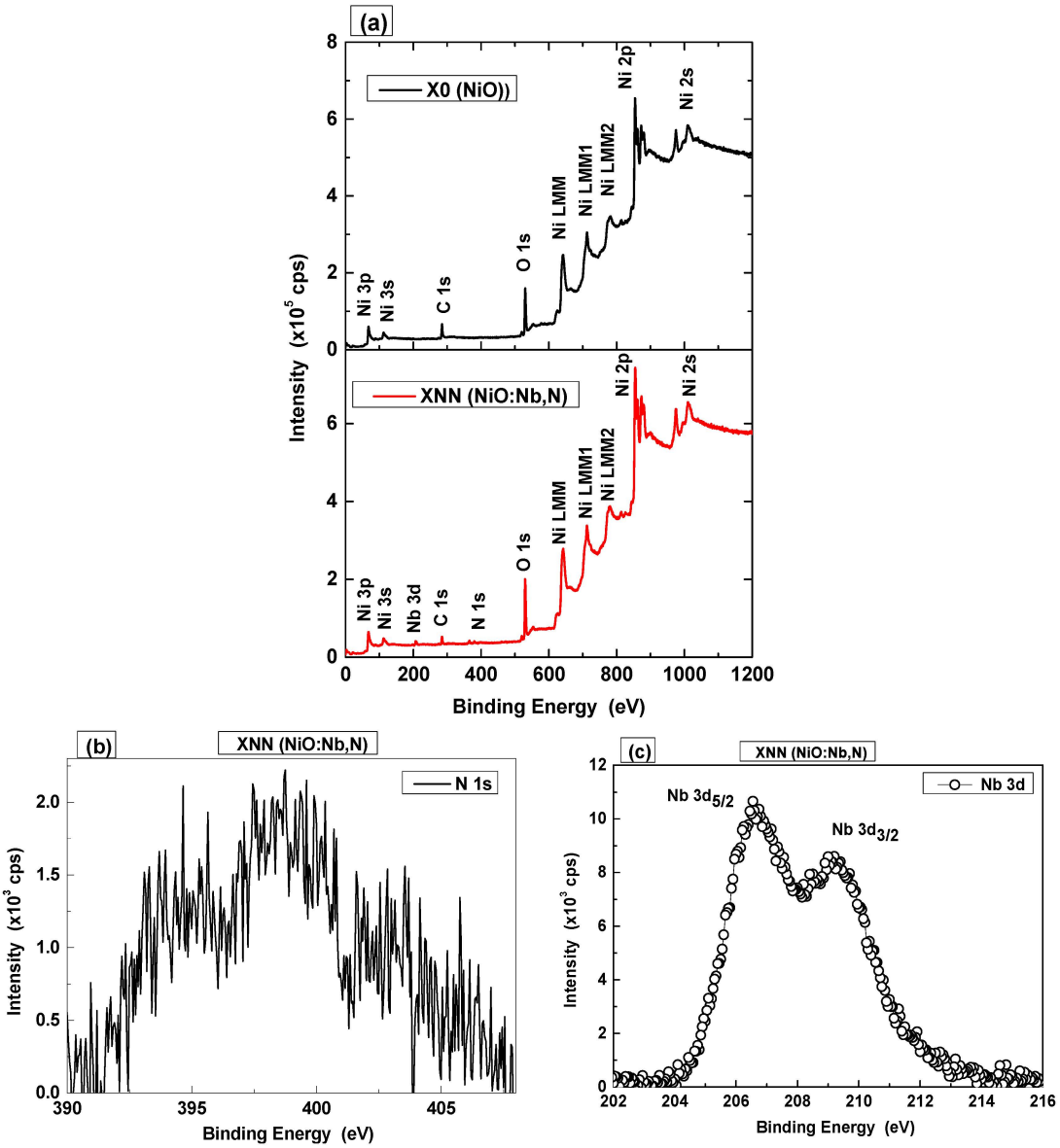

Figure 3. (**a**) Wide-scan XPS spectra of undoped NiO -X0 film and double-doped NiO:(Nb,N)—XNN film. (**b**,**c**) High-resolution N 1s and Nb 3d core levels spectra of double-doped NiO: (Nb,N)—XNN film, respectively.

The effect of the double doping (Nb,N) in the Ni-O structure was examined by XRD measurements. The XRD graphs of both undoped NiO-X0 film and double-doped NiO:(Nb,N)—XNN film, deposited on glass substrates, just after fabrication and after thermal treatment TT1, are shown in Figure 4. The Au metallization pads, which had been applied for performing the electrical characterization of the films, gave rise to diffraction peaks denoted by the asterisks in Figure 4 (Joint Committee of Powder Diffraction Standards (JCPDS) card No: 040-0784). The undoped NiO film just after deposition (Figure 4a) yielded one main diffraction peak at around 42.5° and two more peaks with smaller intensity at around 36.5° and 62.2°. All diffraction peaks were identified as those arising

from (200), (111), and (220) crystallographic planes, respectively, of the cubic NiO phase (JCPDS card No: 04-0835). After the thermal treatment (TT1) of NiO, the diffraction peaks (Figure 4a) became sharper, with higher intensity indicating improvement of crystallinity, while shifting to higher angles indicating a change in strain.

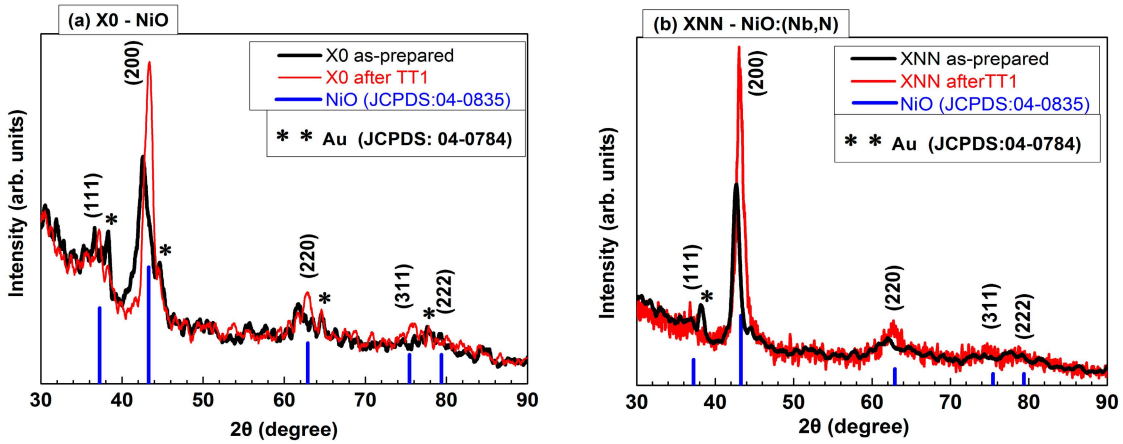

Figure 4. XRD graphs of (**a**) undoped NiO—X0 film and (**b**) doped NiO:(Nb,N) –XNN films deposited on glass substrates just after fabrication and after thermal treatment (TT1).

The crystallographic parameters which were extracted from the XRD patterns, like average crystallite size, lattice strain, and lattice constant, confirmed these observations and have been tabulated in Table 2. It is observed that after TT1 there is almost a 40% increase in average crystallite size, from 5.3 to 7.4 nm, a 30% decrease of lattice strain, and almost 2% decrease of lattice constant from the unheated film. All crystallographic parameters of thermally treated NiO approached those of crystalline NiO (JCPDS card No: 04-0835). As seen in Table 2, the low-temperature growth induced defect-related disorder in the structure and created tensile stress, which was partially relaxed after TT1 leading at the same time to bigger crystallites. By introducing Nb and N as dopants in the Ni-O structure, the films remained polycrystalline single phase NiO, as seen in Figure 4b, without any detectable Nb-related or nitride phases. Improvement of crystallinity was observed after the heat treatment of the films as in the case of undoped NiO. However, the NiO:(Nb,N) films had almost twice the size of crystallites (10 nm) and almost half the lattice strain, than that of the undoped NiO as seen in Table 2. These properties are expected to significantly reduce the scattering of carriers at the grain's or crystallite's boundaries and the trapping into states which can act as non-radiative recombination centers.

Table 2. Crystallographic properties of undoped and double-doped NiO films.

		(200) Peak Position, 2θ (Degree)	Crystallite Size, D (nm)	Lattice Strain, ε ($\times 10^{-3}$)	Lattice Constant (Å)
X0—NiO	**As-prepared**	42.56	5.33	17.7	4.245
	TT1	43.40	7.44	12.4	4.166
XNN—NiO:(Nb,N)	**As-prepared**	42.66	10.07	9.4	4.235
	TT1	43.04	9.13	10.2	4.200

It has been reported [18] that when NiO is made by sputtering in plasma containing N_2 gas as a dopant, the optimum amount of nitrogen in plasma for obtaining films with the largest crystallite size and the smallest lattice stress is (50% Ar + 25% O_2 + 25% N_2). Furthermore, if Nb is used as a dopant in NiO [7], it does not cause significant changes in the Ni-O structure (see Supplementary Materials). By fabricating doped NiO using the optimum amounts of both Nb and N as dopants during deposition, the nitrogen dopant has more drastic effects on improving the structural properties of the resulting double-doped NiO:(Nb,N). The NiO:(Nb,N) film had the biggest crystallites and the minimum

lattice disorder when compared to the undoped film as seen in Table 2. However, the double doping has little effect on the RMS roughness of NiO:(Nb,N) since it appeared slightly smaller than that of the undoped NiO (2.75 nm and 2.85 nm respectively). The SEM and AFM images for the undoped and double-doped NiO films are shown in Figure 5, respectively.

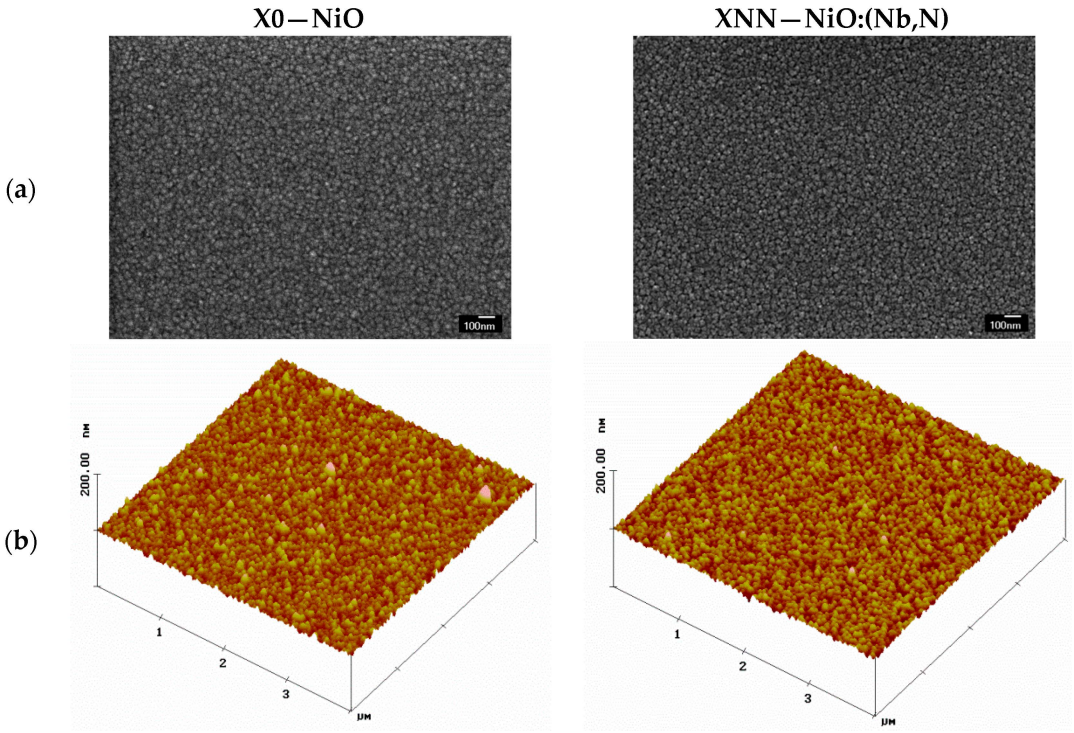

Figure 5. Topography on the same scale of undoped NiO and double-doped NiO:(Nb,N) films deposited on Si substrates: (**a**) SEM and (**b**) AFM images.

It is known that undoped NiO made by sputtering on substrates, kept at room temperature, has a disordered structure and the Ni vacancies create Ni^{+3} ions, which have been associated with the low transmittance of NiO, while thermal treatment improves crystallinity, reduces Ni vacancies and improves transmittance [7,36,37]. This was the case for the NiO films fabricated in this work, where the optical properties of the films followed the structural improvements concerning defects, strain, and transparency. The red curves in Figure 6a show the transmittance of undoped NiO—X0 film just after deposition and after thermal treatment (TT1), where the arrow indicates the increase of the as-prepared film's transmittance at λ = 550 nm after thermal treatment. The NiO shows low visible transmittance (around T = 10% at 550 nm) which is increased after TT1 (T = 55% at 550 nm). Cation and anion co-doping of NiO with Nb and N, respectively, resulted in as-prepared NiO:(Nb,N)—XNN film with significant improvement in transmittance just after deposition (T = 60% at 550nm), which is further enhanced upon thermal treatment (around T = 90% at 550 nm), as indicated by the arrows of Figure 6a. The increase in transmittance of XNN film can be attributed to the reduction of structural disorder and defects as well as to crystallinity enhancement upon doping, which was increased further with the subsequent thermal treatment of the films. Improvement of Ni-O structure with double doping and TT1 resulted in a film through which more photons can be transmitted as they encounter less scattering at defects and grains/crystallites boundaries. This is in very good agreement with the observed increase of crystallites by a factor of two upon double doping, as seen in Table 2. As depicted in Figure 6a, there is no significant change at the onset of transmittance at short wavelengths, indicating that the energy band gap of the films should be expected to be similar. Details about the optical properties extracted from transmittance curves are presented below.

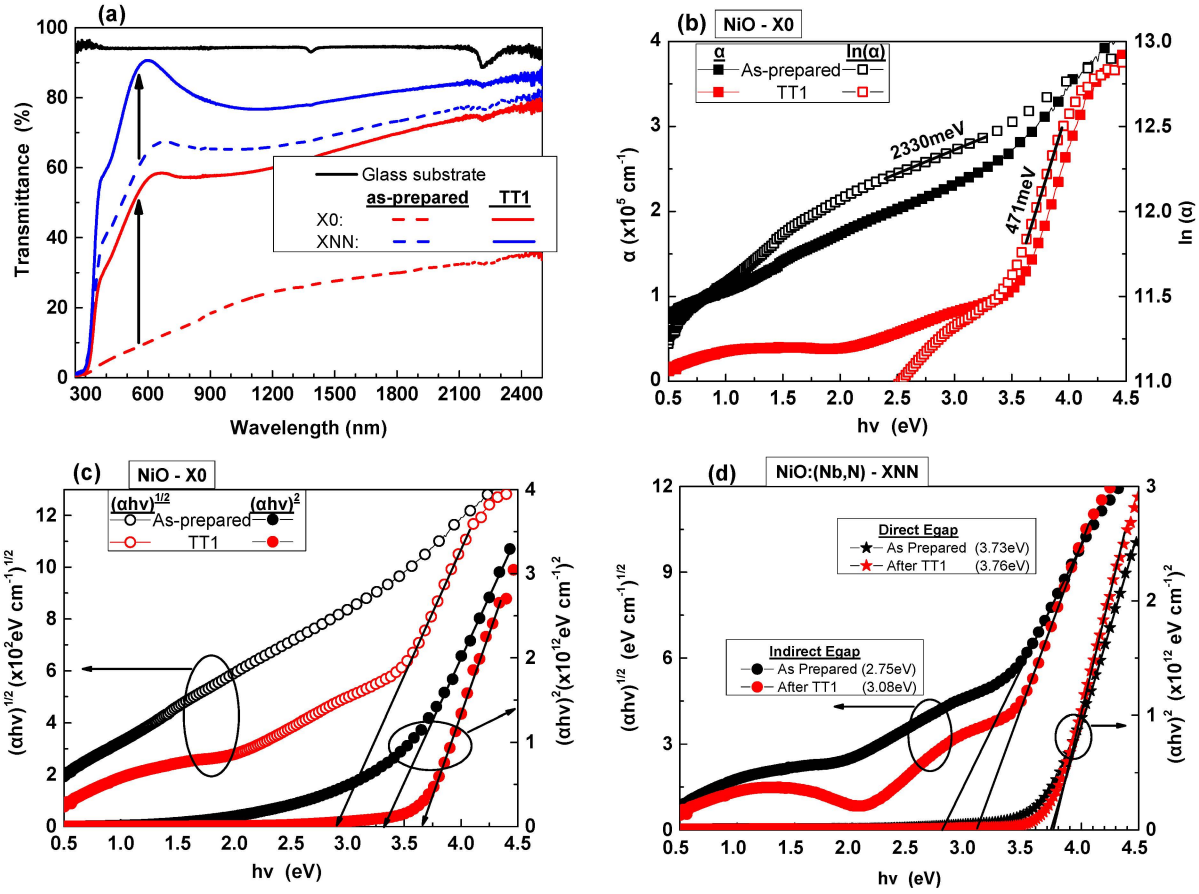

Figure 6. Optical properties of NiO—X0 and NiO:(Nb,N)—XNN films just after deposition and after thermal treatment (TT1): (**a**) UV-Vis-NIR transmittance of X0 and XNN films (the arrows indicate the increase of transmittance at λ = 550 nm after TT1). (**b**) Absorption coefficient, α and ln(α), and (**c**) Tauc plots of X0 film. (**d**) Tauc plots of XNN film.

NiO is generally considered a direct band gap semiconductor associated with transitions from the top of the valence band to the bottom of the conduction band. The direct band gap of thin films is generally determined from spectrophotometric measurements such as UV-Vis-NIR transmittance as described in the Experimental Details section (Equations (3) and (4)). Nevertheless, the band gap of NiO has been reported to be either a direct one ranging from 3.6 to 4 eV or an indirect one ranging from 2.75–2.83 eV [38] or 3.45 eV [39] or having both direct (3.6 eV) and indirect (3.2 eV) band gaps [40]. In addition, the Urbach tail states width, the Urbach energy (E_U), has been associated with non-stoichiometric and disordered Ni-O structures, resulting in shallow localized states near the edge of the valence band. It has been reported that E_U depends on NiO thickness and subsequent thermal treatment, starting from 600 meV for 420 nm thick NiO to 1.7 eV for 700 nm thick NiO, which were subsequently reduced to 500 meV upon annealing [10]. On the contrary, strontium (Sr) doping has been reported to increase E_U from 558 meV for the undoped NiO and 892 meV for NiO:Sr [41].The optical properties of undoped NiO –X0 film before and after TT1 as extracted from transmittance measurements are shown in Figure 6b,c. The absorption coefficient α and the ln(α) for determining Urbach width (E_U) are depicted in Figure 6b, whereas the $(\alpha hv)^2$ and $(\alpha hv)^{1/2}$ plots against photon energy for determining the direct and indirect band gaps (Tauc plots) are seen in Figure 6c. The values of these optical properties have been tabulated in Table 3. It is seen that there is an improvement in the optical properties of undoped X0 film upon annealing due to the improvement of crystallinity and reduction of strain in the Ni-O structure: E_U is reduced and the direct gap is increased. In addition, there is clear evidence of an indirect band gap of undoped

NiO films only after thermal treatment. On the contrary, an indirect band gap could be determined for the double-doped NiO:(Nb,N) film before any heat treatment, which has been plotted in Figure 6d, along with the direct band gap before and after thermal treatment. The optical properties of X0 and XNN films, along with those of the effective TiO_2 film presented in Section 3.1.1, are tabulated in Table 3. It has been reported that the onset of absorption and determination of an indirect band gap from the Tauc plot for nanostructured and polycrystalline films can be associated with phonon-assisted processes as well as to the presence of defects [41]. More experiments along with theoretical modeling are required to clarify and confirm the correlation between the structural defects and the indirect band gap of NiO-based films, as determined from Tauc plots [42].

Table 3. Optical properties of undoped NiO -X0, double-doped NiO:(Nb,N)—XNN and TiO_2 films. E_{gap} = energy band gap, TT1 = thermal treatment, TiO_2 = m-TiO_2/c-TiO_2.

	Direct E_{gap} (eV)		**Indirect E_{gap} (eV)**		**Urbach Width, E_U (meV)**	
	As-Prepared	**TT1**	**As-Prepared**	**TT1**	**As-Prepared**	**TT1**
NiO	3.28	3.67	-	2.97	2330	471
NiO:(Nb,N)	3.73	3.76	2.75	3.08	586	313
TiO_2	3.72		3.28		211	

As can be observed from the results of Table 3, the thermal treatment has a more profound effect on the optical properties of the undoped NiO compared with the double-doped NiO films. It seems that the disorder, strain structure, and the associated defects in the Ni-O structure for the undoped film fabricated at room temperature have been significantly reduced by the dopants, Nb and N in our case. Most of these defects were compensated by the dopants reducing the tail states and increasing the band gap. The width of Urbach states is another important improvement of material properties, as these states appear at the NiO:(Nb,N)-TiO_2 interface, affecting the rectifying output characteristics of the diode [43]. As expected and seen in Table 3, the TiO_2 had the narrowest tail states width (211 meV) and the lowest difference between the direct and indirect band gaps compared with both the NiO:(Nb,N) film (313 meV) and the NiO film (471 eV) after TT1. This observation indicates that the indirect band gap of the films determined from Tauc plots is most likely associated with the presence of defects in the structure, as previously suggested [41]. Single doping of NiO with nitrogen has been correlated with the reduction of Ni vacancies, fewer Ni^{+3} ions, higher visible transmittance, and a larger energy gap [18,19]. On the contrary, when NiO is single doped with Nb, it has been shown not to reduce Ni vacancies but to replace Ni by forming Nb_2O_5 and decreasing the resistivity of the film [7]. Through the doping engineering presented in this work, the combination of optimal double doping by Nb and N resulted in a film with an increased transparency without having a major effect on its conductivity, as will be shown next.

The resistivity of as-prepared undoped NiO was measured to be around 1 Ωcm, whereas upon double doping with Nb and N the NiO:(Nb,N) film exhibited an increase in resistivity to 19 kΩcm. The resistivity of single-doped NiO with nitrogen (NiO:N) has been reported to drastically increase the resistivity of undoped NiO [18,19] whereas single doping with niobium (NiO:Nb) has been shown to have the opposite effect on resistivity [7,44]. Thermal treatment of the films led to a further increase in resistivity to around 2 kΩcm for the undoped NiO and >100 kΩcm for the double-doped NiO:(Nb,N) film. The high resistivity of the NiO:(Nb,N) films did not allow any Hall measurements to be performed for unambiguously confirming the p-type conduction of the film. It can be anticipated that after thermal treatment, the reduction of structural disorder and band gap states (Urbach width) increased both the resistivity and the visible transmittance, along with the energy band gap of the films.

3.2. Properties of NiO:(Nb,N)/TiO_2 Heterostructure

For the fabrication of the transparent photovoltaic device, the NiO:(Nb,N) film was sputtered on top of the spin-coated TiO_2 film, and the heterostructure configuration, NiO:(Nb,N)/m-TiO_2/c-TiO_2/FTO/glass, was thermally treated (TT1) so as to exploit all the structural and optical improvements of the NiO:(Nb,N) layer after heat treatment. Figure 7a shows the topography of the fabricated heterostructure at 30° tilted view and Figure 7b shows the transmittance of the NiO:(Nb,N):TiO_2 heterostructure before and after TT1, along with the transmittance of the substrate (FTO/glass) for comparison reasons. The visible transmittance of the as-prepared NiO:(Nb,N)/TiO_2 heterostructure was increased by 25% after TT1, from T = 45% to around T = 70%, respectively. As described in the Experimental Details section, the mesoporous m-TiO_2 and the compact c-TiO_2 were subjected to thermal treatments at 500 °C during their fabrication. Thus, the improvement of visible transmittance of NiO:N/TiO_2 diode upon thermal treatment is expected to be mainly due to improvement of the structural and optical properties of the NiO:(Nb,N) layer, such as less disorder and lattice strain leading to a narrower Urbach tail and to reduced photon scattering centers.

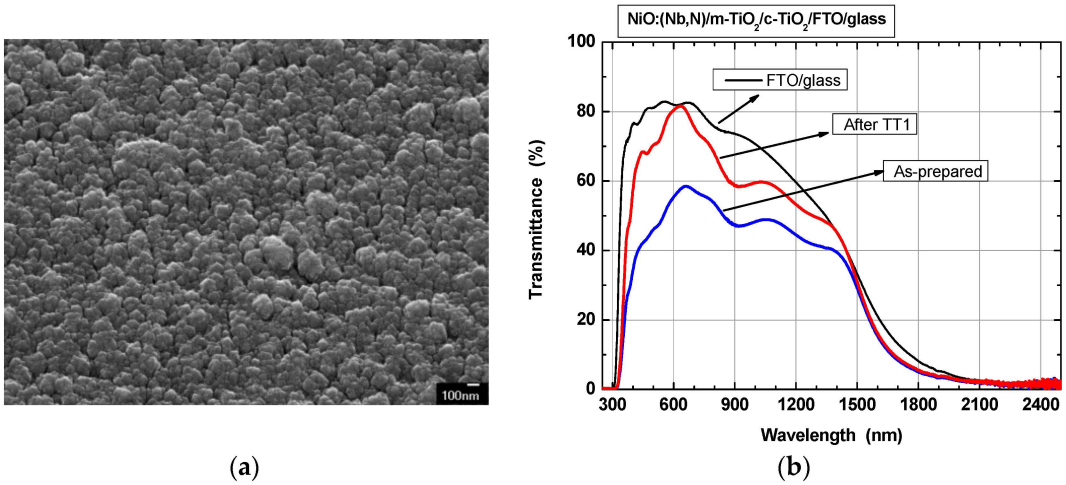

Figure 7. NiO:(Nb,N)/TiO2 heterostructure: (**a**) Topography at 30° tilted view and (**b**) UV-Vis-NIR transmittance before and after TT1, along with the transmittance of substrate (FTO/glass).

The semi-log dark current density-voltage (J_d-V) characteristic of the heat-treated NiO:(Nb,N)/TiO_2 diode is seen in Figure 8a. The heterostructure revealed a rectifying behavior and the rectification ratio (forward current density to reverse current density, J_f/J_r) at ±2V was J_f/J_r = 20. In addition, the dark J-V curve did not exhibit any shift to lower or higher voltages ($V \neq 0$ for the minimum J_d value) indicating that there was not a dipole interlayer formed at the NiO:(Nb,N)-TiO_2 interface, as is commonly observed for most all-oxide diodes [45–48]. Assuming thermionic emission over the barrier for the NiO:(Nb,N)/TiO_2 heterojunction, the parameters of the diode after TT1 were calculated to be [7,18]: saturation current density $J_S = 1 \times 10^{-5}$ A/cm^2, barrier height Φ_b = 0.71 eV, ideality factor n = 8.2, and series resistance R_S = 398 Ω. The diode had relatively high saturation current density (J_S), high series resistance (R_S) but reasonable barrier height (Φ_b) [25]. The high values of J_S and R_S must be attributed to the interface states and the resistivity of the layers forming the diode. However, as the ideality factor was found to be n = 8.2, the transport mechanism of the carriers seems to be dominated by recombination centers at the NiO(Nb,N)-TiO_2 interface and the depletion layers of the heterostructure, as well as tunneling effects [49,50]. It should be emphasized that the NiO:(Nb,N)/TiO_2 heterostructure is a hybrid one, since the n-type layer was made by the chemical method of spin-coating, whereas the p-type layer was formed by the physical vapour deposition technique of sputtering.

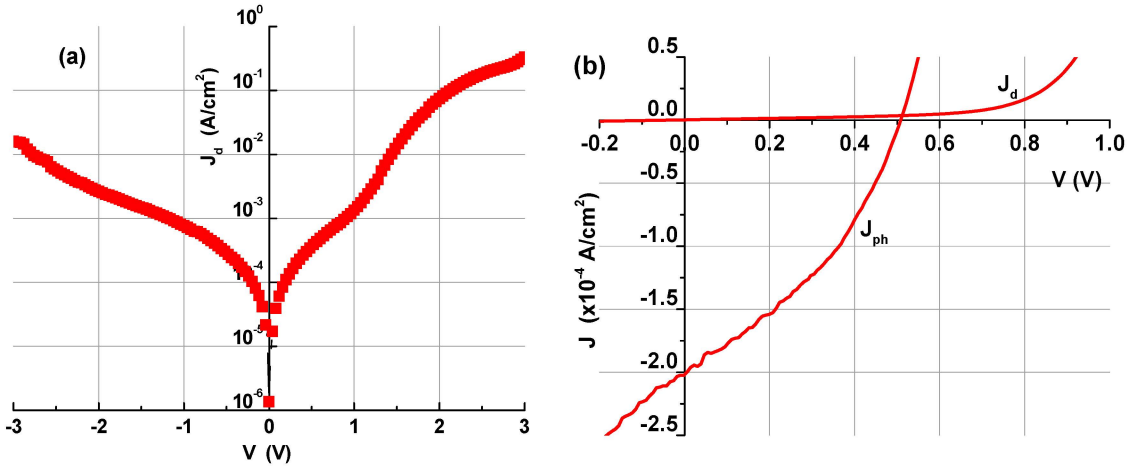

Figure 8. Current density-voltage J-V characteristics of the NiO:(Nb,N)/TiO_2 heterodiode (**a**) semilog characteristics in the dark (J_d-V)) and (**b**) linear characteristics in the dark (J_d) and under UV illumination (J_{ph}).

By illuminating the NiO(Nb,N)/TiO_2heterodiode with UV laser light of 325 nm wavelength from the glass substrate side, photovoltaic behavior was observed, which is seen in Figure 8b. The short-circuit current density was I_{SC} = 200 μA/cm^2 and the open-circuit voltage was V_{OC} = 500 mV. These photovoltaic characteristics of the diode, particularly the V_{OC}, are one of the best reported in the literature for thin film all-oxide NiO/TiO_2 heterostructures. The reports in the literature on NiO/TiO_2 UV-PVs have been tabulated in Table 4 along with the major characteristics/properties of the reported devices. It is worth mentioning that, as seen in Table 4, when a single-doped NiO:Nb formed a junction with a m-TiO_2/c-TiO_2 layer, and was illuminated with the same UV light, the resulting photovoltaic device [7] exhibited inferior properties compared with the double-doped NiO presented in this work.

Table 4. Selected properties of published NiO/TiO_2-based UV-PV thin film devices. SP = Spray Pyrolysis, DC S = DC Sputtering, RTP = Rapid Thermal Processing, T_{VIS} = visible transmittance, P_{IN} = input power, J_{SC} = short circuit current density, I_{SC} = short circuit current, V_{OC} = open circuit voltage.

p/n Layers	Deposition Techn./Thickness p-NiO Layer	n-TiO_2 Layer	T_{VIS} (%)	λ (nm)/P_{IN} (mW/cm^2)	J_{SC} or I_{SC}	Voc (mV)	Year/[Ref.]
NiO/TiO_2	SP	SP	-	Solar Simul./100	16.8 mA	350	2018/[5]
NiO/SnS/TiO_2	DC S/30 nm	DC S/80 nm	40–60	365 nm/70	27.4 μA/cm^2	765	2020/[16]
NiO/TiO_2	DC S	DC S + RTP /100 nm	60–70	365–520 nm/--	0.7–20 μA/cm^2	25–250	2020/[48]
NiO/TiO_2:N	30	DC S + RTP /120 nm	25–45	365–520 nm/6.5	558–66 μA	130	2020/[6]
NiO/TiO_2	DC S	DC S + RTP /350 nm	40–55	365 nm/30	7–8 mA/cm^2	300–500	2021/[47]
NiO:Nb/ m-TiO_2/c-TiO_2	RF MS/150	Spin coating /240 nm	55–65	325 nm/710	1.4 μA/cm^2	200	2023/[7]
NiO:(Nb,N)/ m-TiO_2/c-TiO_2	RF MS/130	Spin coating /240 nm	70–80	325 nm/710	200 μA/cm^2	500	2024/This work

There have been previous reports on double doping of NiO with either anion-cation dopants such as NiO:(Fe,F) [51], NiO:(Cu,N) [52], or cation-cation dopants such as NiO:(Zn,La) [53], NiO:(Li,Mg) [54], NiO:(Fe,Co) [55], NiO:(Zn,Mg) [56], NiO:(Pb,Ir) [57] for enhancing its properties as electrode, catalyst, dielectric, or magnet. However, it is the first time that the effect of anion and cation co-doping of NiO has been explored to show enhanced ultraviolet photovoltaic performance when forming a p/n heterojunction with TiO_2. The photovoltaic performance of NiO:(Nb,N)/TiO_2 is very promising, particularly regarding the V_{OC} of the device. Nevertheless, further improvements on the output characteristics of the UV-PV heterojunction can be realized

by making a few design and fabrication optimizations, some of which are: (i) fabricate an all-sputtered NiO:(Nb,N)/TiO_2 heterostructure instead of a hybrid one, (ii) introduce an interlayer between the NiO-TiO_2 interface to enhance the built-in electric field, (iii) reduce the thickness of the NiO:(Nb,N) and TiO_2 layers, so as to improve the resistivity of the layers and reduce scattering losses, and (iv) illuminate the UV-PV from the NiO side so as to eliminate loss of photons due to absorption in the TiO_2 bi-layer, as seen in Figure 2b and Table 3, when illuminated from the substrate. It is anticipated that these modifications will eliminate the NiO:(Nb,N)-TiO_2 interface states, improve the dark parameters of the diode, particularly J_S and Φ_b, and subsequently the behavior of the diode under illumination (J_{SC} and V_{OC}).

4. Conclusions

A transparent NiO:(Nb,N)/TiO_2heterodiode was fabricated by employing sputtered double-doped NiO:(Nb,N) and spin-coated TiO_2 as p-type and n-type layers, respectively. The reference undoped NiO was fabricated by sputtering a Ni target in plasma containing 50% Ar and 50% O_2. The Nb dopant was introduced in the Ni-O structure by placing Nb pellets on the Ni target and the N dopant was introduced by sputtering the composite Ni-Nb target in plasma by substituting half of O_2 with N_2 gas (50% Ar, 25% O_2, and 25% N_2). All films were deposited on room temperature substrates. Upon Nb and N doping, the O-rich undoped NiO film became less disordered and more transparent. The structural disorder was further reduced and transmittance increased by thermal treatment of the NiO:(Nb,N) films. The direct and indirect band gaps of NiO:(Nb,N), as well as the sub-gap states, the Urbach tail states, were correlated with the existence of a niobium and nitrogen Ni-O structure. The thermally treated NiO:(Nb,N) film revealed a direct band gap of 3.76 eV, an indirect band gap of 3.08 eV and an Urbach energy (tail states) width of 313 meV. The heterojunction was formed on a TiO_2 bi-layer, namely a spin-coated mesoporous TiO_2 on top of a compact-TiO_2, using FTO/glass as substrate. The NiO:(Nb,N)/m-TiO_2/c-TiO_2/FTO/glass heterostructure exhibited a visible transmittance of around 80% and showed rectification properties, which were analyzed by employing the I-V method. Upon illumination with UV light, the heterodiode revealed photovoltaic behavior with a short circuit current density of 0.2 mA/cm^2 and an open-circuit voltage of 500 mV. The double doping of NiO with anion (N) and cation (Nb) dopants can be used as UV-PV for solar cells, smart windows, and other optoelectronic applications.

Supplementary Materials: The following supporting information can be downloaded at: https://www.mdpi.com/article/10.3390/cryst14070629/s1, Figure S1: UV-Vis-NIR transmittance of the undoped NiO film, the single doped NiO filmsNiO:Nb [7], NiO:N [18,19]) and the double doped NiO film (NiO:(Nb,N): (a) just after deposition (as-prepared) and (b) after thermal treatment (TT1 = 300 °C, 15 min, N2).; Table S1: Details of the structural and optical properties of the as-prepared undoped NiO film, the single doped NiO films (NiO:Nb [7], NiO:N [18,19]) and the double doped NiO film (NiO:(Nb,N).

Author Contributions: Conceptualization, E.A.; methodology, E.A.; validation, C.A; formal analysis, C.A.; investigation, C.A., E.G.M., M.A. and K.T.; resources, E.G.M. and N.T.P.; data curation, C.A.; writing—original draft preparation, E.A.; writing—review and editing, N.T.P., E.G.M., M.A., K.T. and E.A.; supervision, E.A.; funding acquisition, E.A. and N.T.P. All authors have read and agreed to the published version of the manuscript.

Funding: This work was partially supported by the projects "Materials and Processes for Energy and Environment Applications-AENAO" (MIS 5002556) and "NANOTANDEM" (MIS 5029191) co-financed by Greece and EU (European Regional Development Fund).

Data Availability Statement: The raw data supporting the conclusions of this article will be made available by the authors on request.

Acknowledgments: We are grateful to E. Spanakis of Materials Science & Engineering Department of the University of Crete for performing the XPS experiments.

Conflicts of Interest: The authors declare no conflicts of interest.

References

1. Lemmet, S. *Buildings and Climate Change: Summary for Decision-Makers Sustainable Buildings & Climate Initiative*; United Nations Environmental Programme: Paris, France, 2009; pp. 1–62.
2. Yang, L.; Yan, H.; Lam, J.C. Thermal comfort and building energy consumption implications—A review. *Appl. Energy* **2014**, *115*, 164–173. [CrossRef]
3. Wang, Z.; Wang, X.; Cong, S.; Geng, F.; Zhao, Z. Fusing electrochromic technology with other advanced technologies: A new roadmap for future development. *Mater. Sci. Eng. R* **2020**, *140*, 100524. [CrossRef]
4. Lunt, R.R. Theoretical limits for visibly transparent photovoltaics. *Appl. Phys. Lett.* **2012**, *101*, 043902. [CrossRef]
5. Ukoba, K.O.; Inambao, F.L.; Eloka-Eboka, A.C. Fabrication of affordable and sustainable solar cells using NiO/TiO_2 P-N heterojunction. *Int. J. Photoenergy* **2018**, *7*, 6062390. [CrossRef]
6. Abbas, S.; Kim, J. All-metal oxide transparent photodetector for broad responses. *Sens. Actuators A* **2020**, *303*, 111835. [CrossRef]
7. Aivalioti, C.; Manidakis, E.G.; Pelekanos, N.T.; Androulidaki, M.; Tsagaraki, K.; Viskadourakis, Z.; Spanakis, E.; Aperathitis, E. Niobium-doped NiO as p-type nanostructured layer for transparent photovoltaics. *Thin Solid Film.* **2023**, *778*, 139910. [CrossRef]
8. Xu, J.; Cao, R.; Shi, S.; Li, L.; Zhu, K.; Su, Y. Self-powered ultraviolet photodetectors based on match like quasi one- dimensional n-TiO_2/p-NiO core-shell heterojunction arrays with NiO layer sputtered at different power. *J. Alloys Compd.* **2022**, *928*, 167126. [CrossRef]
9. Kumar, N.; Patel, M.; Nguyen, T.T.; Kim, S.; Kim, J. Effect of TiO_2 layer thickness of TiO_2/NiO transparent photovoltaics. *Prog. Photovolt. Res. Appl.* **2021**, *29*, 943–952. [CrossRef]
10. Klochko, N.P.; Kopach, V.R.; Tyukhov, I.I.; Zhadan, D.O.; Klepikova, K.S.; Khrypunova, G.S.; Petrushenko, S.I.; Lyubov, V.M.; Kirichenko, M.V.; Dukarov, S.V.; et al. Metal oxide heterojunction (NiO/ZnO) prepared by low temperature solution growth for UV-photodetector and semi-transparent solar cell. *Sol. Energy* **2018**, *164*, 149–159. [CrossRef]
11. Nguyen, T.T.; Patel, M.; Kim, J.W.; Lee, W.; Kim, J. Functional TiO_2 interlayer for all transparent metal-oxide photovoltaics. *J. Alloys Compd.* **2020**, *816*, 152602. [CrossRef]
12. Grundmann, M.; Klüpfel, F.; Karsthof, R.; Schlupp, P.; Schein, F.-L.; Splith, D.; Yang, C.; Bitter, S.; von Wenckstern, H. Oxide bipolar electronics: Materials, devices and circuits. *J. Phys. D Appl. Phys.* **2016**, *49*, 213001. [CrossRef]
13. Karsthof, R.; Racke, P.; von Wenckstern, H.; Grundmann, M. Semi-transparent NiO/ZnO UV photovoltaic cells. *Phys. Status Solidi A* **2016**, *213*, 30–37. [CrossRef]
14. Ghosh, S.; Patel, M.; Lee, J.; Kim, J. All-Oxide Transparent Photodetector Array for Ultrafast Response through Self-Powered Excitonic Photovoltage Operation. *Small* **2023**, *19*, 2301702. [CrossRef] [PubMed]
15. Hovel, H.J.; Willardson, R.K.; Beer, A.C. *Solar Cells*; Chapter 2, Semiconductors and Semimetals Series, 11; Academic Press: New York, NY, USA, 1976; ISBN 10: 0127521119, ISBN 13: 9780127521114.
16. Patel, M.; Nguyen, T.T.; Kumar, M.; Ban, D.K.; Won, D.; Zhao, M.; Kim, J.; Kim, Y.K.; Yang, H.; Wonger, C.P. 2D layer-embedded transparent photovoltaics. *Nano Energy* **2020**, *68*, 104328. [CrossRef]
17. Fu, W.; Pan, J.; Niu, J.; Fu, Y.; Xiao, G.; Wang, J.; Zheng, Y.; Li, C. A transparent photovoltaic device of NiO/MgO quantum dots/TiO_2 arrays pn junction with carrier injection of MgO QDs. *J. Mater. Sci. Mater. Electron.* **2022**, *33*, 652–662. [CrossRef]
18. Aivalioti, C.; Papadakis, A.; Manidakis, E.; Kayambaki, M.; Androulidaki, M.; Tsagaraki, K.; Pelekanos, N.T.; Stoumpos, C.; Modreanu, M.; Crăciun, G.; et al. Transparent All-Oxide Hybrid NiO:N/TiO_2 Heterostructure for Optoelectronic Applications. *Electronics* **2021**, *10*, 988. [CrossRef]
19. Aivalioti, C.; Papadakis, A.; Manidakis, E.; Kayambaki, M.; Androulidaki, M.; Tsagaraki, K.; Pelekanos, N.T.; Stoumpos, C.; Modreanu, M.; Craciun, G.; et al. An Assessment of Sputtered Nitrogen-Doped Nickel Oxide for all-Oxide Transparent Optoelectronic Applications: The Case of Hybrid NiO:N/TiO_2 Heterostructure. In *Recent Trends in Chemical and Material Sciences*; B P International: London, UK, 2022; Volume 6, pp. 86–111, Chapter 8. [CrossRef]
20. Yang, D.; Zhou, X.; Yang, R.; Yang, Z.; Yu, W.; Wang, X.; Li, C.; Liu, S.; Chang, R.P.H. Surface optimization to eliminate hysteresis for record efficiency planar perovskite solar cells. *Energy Environ. Sci.* **2016**, *9*, 3071. [CrossRef]
21. Gagaoudakis, E.; Michail, G.; Kampylafka, V.; Tsagaraki, K.; Aperathitis, E.; Moschovis, K.; Binas, V.; Kiriakidis, G. Room Temperature p-Type NiO Nanostructure Thin Film Sensor for Hydrogen and Methane Detection. *Sens. Lett.* **2017**, *15*, 663–667. [CrossRef]
22. Nath, D.; Singh, F.; Das, R. X-ray diffraction analysis by Williamson-Hall, Halder-Wagner and size-strain plot methods of CdSe nanoparticles- a comparative study. *Mat. Chem. Phys.* **2020**, *239*, 122021. [CrossRef]
23. Pankove, J. *Optical Processes in Semiconductors*; Dover Publications: New York, NY, USA, 1971; p. 87, Chapter 4.
24. Davis, E.A.; Mott, N.F. Conduction in non-crystalline systems V. Conductivity, optical absorption and photoconductivity in amorphous semiconductors. *Philos. Mag.* **1970**, *22*, 0903–0922. [CrossRef]
25. Sze, S.M. *Physics of Semiconductor Devices*, 2nd ed.; John Wiley and Sons Ltd.: Hoboken, NJ, USA, 1981; ISBN 13: 978-0471098379.
26. Bi, Z.; Liu, X.; Zhang, Y.; Zhang, Y.; Ma, Y.; Chen, Y.; Zhou, J.; Ruan, S. An MSM photodetector based on an InGaO/TiO_2heterojunction for high-performance UV detection. *Appl. Phys. Lett.* **2024**, *124*, 022101. [CrossRef]
27. Naas, L.-A.; Bouaouina, B.; Bensouici, F.; Mokeddem, K.; Abaidia, S.E. Effect of TiN thin films deposited by oblique angle sputter deposition on sol-gel coated TiO_2 layers for photocatalytic applications. *Thin Solid Film.* **2024**, *793*, 140275. [CrossRef]
28. Shalaan, E.; Ibrahim, E.; Al-Marzouki, F.; Al-Dossari, M. Observation of mixed types of energy gaps in some II–VI semi-conductors nanostructured films: Towards enhanced solar cell performance. *Appl. Phys. A* **2020**, *126*, 852. [CrossRef]

29. Choudhury, B.; Choudhury, A. Oxygen defect dependent variation of band gap, Urbach energy and luminescence property of anatase, anatase–rutile mixed phase and of rutile phases of TiO_2 nanoparticles. *Phys. E* **2014**, *56*, 364–371. [CrossRef]
30. Kavan, L. Electrochemistry and band structure of semiconductors (TiO_2, SnO_2, ZnO): Avoiding pitfalls and textbook errors. *J. Solid State Electrochem.* **2024**, *28*, 829–845. [CrossRef]
31. Mor, G.K.; Varghese, O.K.; Paulose, M.; Shankar, K.; Grimes, C.A. A review on highly ordered, vertically oriented TiO_2na-notube arrays: Fabrication, material properties, and solar energy applications. *Sol. Energy Mater. Sol. Cells* **2006**, *90*, 2011–2075. [CrossRef]
32. Keraudy, J.; Ferrec, A.; Richard-Plouet, M.; Hamon, J.; Goullet, A.; Jouan, P.-Y. "Nitrogen doping on NiO by reactive magne-tron sputtering: A new pathway to dynamically tune the optical and electrical properties. *Appl. Surf. Sci.* **2017**, *409*, 77–84. [CrossRef]
33. Himmerlich, M.; Koufaki, M.; Ecke, G.; Mauder, C.; Cimalla, V.; Schaefer, J.A.; Kondilis, A.; Pelekanos, N.T.; Modreanu, M.; Krischok, S.; et al. Effect of Annealing on the Properties of Indium−Tin−Oxynitride Films as Ohmic Contacts for GaN-Based Optoelectronic Devices. *ACS Appl. Mater. Interfaces* **2009**, *1*, 1451–1456. [CrossRef]
34. Jin, S.; Guan, W.; Tsang, C.-W.; Yan, D.Y.S.; Chan, C.-Y.; Liang, C. Enhanced Hydroconversion of Lignin-Derived Oxy-gen-Containing Compounds Over Bulk Nickel Catalysts Though Nb_2O_5 Modification. *Catal. Lett.* **2017**, *147*, 2215–2224. [CrossRef]
35. Qiu, L.; Zhang, S.; Huang, J.; Wang, C.; Zhao, R.; Qu, F.; Wang, P.; Yang, M. Highly selective and sensitive xylene sensors based on Nb-doped NiO nanosheets. *Sens. Actuators B. Chem.* **2020**, *308*, 127520. [CrossRef]
36. Hwang, J.D.; Ho, T.H. Effects of oxygen content on the structural, optical, and electrical properties of NiO films fabricated by radio-frequency magnetron sputtering. *Mat. Sci. Semicond. Process.* **2017**, *71*, 396–400. [CrossRef]
37. Tian, Y.; Gong, L.; Qi, X.; Yang, Y.; Zhao, X. Effect of Substrate Temperature on the Optical and Electrical Properties of Nitrogen-Doped NiO Thin Films. *Coatings* **2019**, *9*, 634. [CrossRef]
38. Peng, W.B.; Zhou, Y.J.; Xiang, G.J.; Liu, Y.; Zhang, J.H.; Zhang, J.M.; Huang, H.X.; Mei, M.Y.; Wang, H.; Zhao, Y. Preparation of AlN thin film and the impacts of AlN buffer layer on the carrier transport properties of p-NiO/n-InN heterojunction by magnetron sputtering. *Mater. Sci. Semicond. Process.* **2022**, *141*, 106417. [CrossRef]
39. Lin, C.-W.; Chung, W.-C.; Zhang, Z.-D.; Hsu, M.-C. P-channel transparent thin-film transistor using physical-vapor-deposited NiO layer. *Jpn. J. Appl. Phys.* **2018**, *57*, 01AE01. [CrossRef]
40. Park, S.G.; Lee, K.H.; Lee, J.-H.; Bang, G.; Kim, J.; Park, H.J.; Oh, M.S.; Lee, S.; Kim, Y.-H.; Kim, Y.-M.; et al. Improved polaronic transport under a strong Mott–Hubbard interaction in Cu substituted NiO. *Inorg. Chem. Front.* **2020**, *7*, 853–858. [CrossRef]
41. Siddique, M.N.; Ahmed, A.; Tripathi, P. Enhanced optical properties of pure and Sr doped NiO nanostructures: A compre-hensive study. *Optik* **2019**, *185*, 599–608. [CrossRef]
42. Zanatta, A.R. Revisiting the optical bandgap of semiconductors and the proposal of a unified methodology to its determination. *Sci. Rep.* **2019**, *9*, 11225. [CrossRef]
43. Gong, H.; Chen, X.; Xu, Y.; Chen, Y.; Ren, F.; Liu, B.; Gu, S.; Zhang, R.; Ye, J. Band Alignment and Interface Recombination in NiO/β-Ga_2O_3 Type-II p-n Heterojunctions. *IEEE Trans. Electron Devices* **2020**, *67*, 3341–3347. [CrossRef]
44. Popescu, I.; Skoufa, Z.; Heracleous, E.; Lemonidou, A.; Marcu, I.-C. A study by electrical conductivity measurements of the semiconductive and redox properties of Nb-doped NiO catalysts in correlation with the oxidative dehydrogenation of ethane. *Phys. Chem. Chem. Phys.* **2015**, *17*, 8138–8147. [CrossRef]
45. Polyakov, A.Y.; Smirnov, N.B.; Shchemerov, I.V.; Vasilev, A.A.; Kochkova, A.I.; Chernykh, A.V.; Lagov, P.B.; Pavlov, Y.S.; Stolbunov, V.S.; Kulevoy, T.V.; et al. Crystal orientation dependence of deep level spectra in proton irradiated bulk β-Ga_2O_3. *J. Appl. Phys.* **2021**, *130*, 035701. [CrossRef]
46. Karsthof, R.; von Wenckstern, H.; Zúniga-Pérez, J.; Deparis, C.; Grundmann, M. Nickel Oxide–Based Heterostructures with Large Band Offsets. *Phys. Status Solidi B* **2020**, *257*, 1900639. [CrossRef]
47. Vygranenko, Y.; Wang, K.; Nathan, A. Low leakage heterostructure ultraviolet sensor. *Appl. Phys. Lett.* **2006**, *89*, 172105. [CrossRef]
48. Nguyen, T.T.; Patel, M.; Kim, J. All-inorganic metal oxide transparent solar cells. *Sol. Energy Mater. Sol. Cells* **2020**, *217*, 110708. [CrossRef]
49. Hwang, J.D.; Jiang, C.I.; Hwang, S.B. P-NiO/n-ZnO heterojunction photodiodes with an MgZnO/ZnO quantumwell insertion layer. *Mater. Sci. Semicond. Process.* **2020**, *105*, 104711. [CrossRef]
50. Dawidowski, W.; Sciana, B.; Bielak, K.; Mikolášek, M.; Drobný, J.; Serafinczuk, J.; Lombardero, I.; Radziewicz, D.; Kijaszek, W.; Kósa, A.; et al. Analysis of Current Transport Mechanism in AP-MOVPE Grown GaAsN p-i-n Solar Cell. *Energies* **2021**, *14*, 4651. [CrossRef]
51. Wang, J.; Ren, Y.; Wang, P. (Fe, F) co-doped nickel oxyhydroxide for highly efficient oxygen evolution reaction. *J. Mater. Chem. A* **2023**, *11*, 4619. [CrossRef]
52. Wen, C.-K.; Xin, Y.-Q.; Chen, S.-C.; Chuang, T.-H.; Chen, P.-J.; Sun, H. Comparison of microstructural and optoelectronic properties of NiO:Cu thin films deposited by ion-beam assisted rf sputtering in different gas atmospheres. *Thin Solid Film.* **2019**, *677*, 103–108. [CrossRef]
53. Raj, I.L.P.; Valanarasu, S.; Ade, R.; Bitla, Y.; Mohanraj, P.; Ganesh, V.; Yahia, I.S. Enhancing the ultraviolet photosensingproperties of nickel oxide thin films by Zn–La co-doping. *Ceram. Int.* **2022**, *48*, 5026–5034. [CrossRef]
54. Dong, D.; Wang, W.; Barnabe, A.; Presmanes, L.; Rougier, A.; Dong, G.; Zhang, F.; Yu, H.; He, Y.; Dia, X. Enhanced electrochromism in short wavelengths for NiO:(Li,Mg) films in full inorganic device ITO/NiO:(Li, Mg)/Ta_2O_5/WO_3/ITO. *Electrochim. Acta* **2018**, *263*, 277–285. [CrossRef]

55. Abbas, H.; Nadeem, K.; Munir, S.; Ahmed, U.; Usman, M.; Kostylev, M. Fe–Co co-doping effects on antiferromagnetic core of NiO nanoparticles. *Ceram. Int.* **2022**, *48*, 3435–3447. [CrossRef]
56. Ahmed, A.A.A.; Alahsab, E.A.A.; Abdulwahab, A.M. The influence of Zn and Mg doping on the structural and optical properties of NiO nano-structures for optoelectronic applications. *Results Phys.* **2021**, *22*, 103938. [CrossRef]
57. El Sayed, A.M. Exploring the morphology, optical and electrical properties of nickel oxide thin films under lead and iridium doping. *Phys. B* **2021**, *600*, 412601. [CrossRef]